Coherent Interferometry Algorithms for Photoacoustic Imaging

Habib Ammari* Elie Bretin† Josselin Garnier‡ Vincent Jugnon†

November 8, 2010

Abstract

The aim of this paper is to develop new Coherent Interferometry (CINT) algorithms to correct the effect of an unknown cluttered sound speed (random fluctuations around a known constant) on photoacoustic images. By back-projecting the correlations between the pre-processed pressure measurements, we show that we are able to provide statistically stable photo-acoustic images. The pre-processing is exactly in the same way as when we use the circular or the line Radon inversion to obtain photo-acoustic images. Moreover, we provide a detailed stability and resolution analysis of the new CINT-Radon algorithms. We also present numerical results to illustrate their performance and to compare them with Kirchhoff-Radon migration functionals.

AMS subject classifications. 65R32, 44A12, 35R60

Key words. Imaging, migration, interferometry, random media, resolution, stability

1 Introduction

In photoacoustic imaging, optical energy absorption causes thermo-elastic expansion of the tissue, which leads to the propagation of a pressure wave. This signal is measured by transducers distributed on the boundary of the object, which in turn is used for imaging optical properties of the object. The major contribution of photo-acoustic imaging is to provide images of optical contrasts (based on the optical absorption) with the resolution of ultrasound [21]. The absorbed energy density is related to the optical absorption coefficient distribution through a model for light propagation such as the diffusion approximation or the radiative transfer equation. Although the problem of reconstructing the absorption coefficient from the absorbed energy is nonlinear, efficient techniques can be designed, specially in the context of small absorbers [2]. The absorbed optical energy density is the initial condition in the acoustic wave equation governing the pressure. If the medium is acoustically homogeneous and has the same acoustic properties as the free space, then the boundary of the object

*Department of Mathematics and Applications, Ecole Normale Supérieure, 45 Rue d'Ulm, 75005 Paris, France (habib.ammari@ens.fr).

†Centre de Mathématiques Appliquées, CNRS UMR 7641, Ecole Polytechnique, 91128 Palaiseau, France (bretin, jugnon@cmap.polytechnique.fr).

‡Laboratoire de Probabilités et Modèles Aléatoires & Laboratoire Jacques-Louis Lions, site Chevaleret, case 7012, Université Paris VII, 75205 Paris Cedex 13, France (garnier@math.jussieu.fr).

plays no role and the absorbed energy density can be reconstructed from measurements of the pressure wave by inverting a spherical or a circular Radon transform [15, 16, 13, 14].

Recently, we have been interested in reconstructing initial conditions for the wave equation with *constant* sound speed in a bounded domain. In [1, 3], we developed a variety of inversion approaches which can be extended to the case of variable but known sound speed and can correct for the effect of attenuation on image reconstructions. However, the situation of interest for medical applications is the case where the sound speed is perturbed by an unknown clutter noise. This means that the speed of sound of the medium is randomly fluctuating around a known value. In this situation, waves undergo partial coherence loss [12] and the designed algorithms assuming a constant sound speed may fail.

Interferometric methods for imaging have been considered in [9, 19, 20]. Coherent interferometry (CINT) was introduced and analyzed in [5, 6]. While classical methods back-propagate the recorded signals directly, CINT is an array imaging method that first computes cross-correlations of the recorded signals over appropriately chosen space-frequency windows and then back-propagates the local cross-correlations. As shown in [5, 6, 7, 8], CINT deals well with partial loss of coherence in cluttered environments.

In the present paper, combining the CINT method for imaging in clutter together with a reconstruction approach for extended targets by Radon inversions, we propose CINT-Radon algorithms for photoacoustic imaging in the presence of random fluctuations of the sound speed. We show that these new algorithms provide statistically stable photoacoustic images. We provide a detailed analysis for their stability and resolution and numerically illustrate their performance.

The paper is organized as follows. In Section 2 we formulate the inverse problem of photoacoustics and describe the clutter noise considered for the sound speed. In Section 3 we recall the reconstruction using the circular Radon transform when the sound speed is constant and describe the original CINT algorithm. We then propose a new CINT approach which consists in pre-processing the data (in the same way as for the circular Radon inversion) before back-projecting their correlations. Section 4 is devoted to the stability analysis of this new algorithm. Section 5 adapts the results presented in Sections 3 and 4 to the case of a bounded domain. We make a parallel between the filtered back-projection of the *circular* Radon inversion in free space and of the *line* Radon inversion when we have boundary conditions. Both algorithms end with a back-projection step. We propose to back-project the correlations between the (pre-processed) data in the same way as in Section 3. The paper ends with a short discussion.

2 Problem Formulation

In photoacoustics, a pressure wave $p(\boldsymbol{x}, t)$ is generated by an electromagnetic energy deposit $p_0(\boldsymbol{x})$:

$$\begin{cases} \dfrac{\partial^2 p}{\partial t^2}(\boldsymbol{x}, t) - c(\boldsymbol{x})^2 \Delta p(\boldsymbol{x}, t) = 0, \\ p(\boldsymbol{x}, 0) = p_0(\boldsymbol{x}), \quad \dfrac{\partial p}{\partial t}(\boldsymbol{x}, 0) = 0. \end{cases}$$

The imaging problem is to reconstruct the initial value of the pressure p_0 from boundary measurements. Most of the reconstruction algorithms assume constant (or known) sound speed. However, in real applications, the sound speed is not perfectly known. It seems more

relevant to consider that it fluctuates randomly around a known distribution. For simplicity, we will consider the model with random fluctuations around a constant:

$$\frac{1}{c(\boldsymbol{x})^2} = \frac{1}{c_0^2}\Big(1 + \sigma_c \mu\big(\frac{\boldsymbol{x}}{x_c}\big)\Big), \tag{2.1}$$

where μ is a normalized stationary random process, x_c is the correlation length of the fluctuations of c and σ_c is their relative standard deviation.

3 Imaging Algorithms

Consider the two-dimensional case. Define the Fourier transform by

$$\hat{f}(\omega) = \int_{\mathbb{R}} f(t) e^{i\omega t}\, dt, \qquad f(t) = \frac{1}{2\pi}\int_{\mathbb{R}} \hat{f}(\omega) e^{-i\omega t}\, d\omega. \tag{3.1}$$

In free space, it is possible to link the measurements of the pressure waves $p(\boldsymbol{y}, t)$ on the boundary $\partial\Omega$ to the circular Radon transform of the initial condition $p_0(\boldsymbol{x})$ as follows [11]:

$$\mathcal{R}_\Omega[p_0](\boldsymbol{y}, r) = \mathcal{W}[p](\boldsymbol{y}, r), \quad \boldsymbol{y} \in \partial\Omega, \quad r \in \mathbb{R}^+,$$

where the circular Radon transform is defined by

$$\mathcal{R}_\Omega[p_0](\boldsymbol{y}, r) := \int_{\mathbb{S}^1} r p_0(\boldsymbol{y} + r\boldsymbol{\theta}) d\sigma(\boldsymbol{\theta}), \quad \boldsymbol{y} \in \partial\Omega, \quad r \in \mathbb{R}^+,$$

and

$$\mathcal{W}[p](\boldsymbol{y}, r) := 4r \int_0^s \frac{p(\boldsymbol{y}, t/c_0)}{\sqrt{s^2 - t^2}}\, dt, \quad \boldsymbol{y} \in \partial\Omega, \quad r \in \mathbb{R}^+.$$

Here $\mathbb{S}^1$ denotes the unit circle. When Ω is the unit disk with center at $\mathbf{0}$ and radius $X_0 = 1$, in order to find p_0 we can use the following exact inversion formula [17]:

$$p_0 = \frac{1}{4\pi^2}\mathcal{R}_\Omega^\star \mathcal{B}\mathcal{W}[p], \tag{3.2}$$

where $\mathcal{R}_\Omega^\star$ (the adjoint of the circular Radon transform) is a back-projection operator given by

$$\mathcal{R}_\Omega^\star[f](\boldsymbol{x}) = \int_{\partial\Omega} f(\boldsymbol{y}, |\boldsymbol{x} - \boldsymbol{y}|) d\sigma(\boldsymbol{y}) = \frac{1}{2\pi}\int_{\partial\Omega}\int_{\mathbb{R}} \hat{f}(\boldsymbol{y}, \omega) e^{-i\omega|\boldsymbol{x}-\boldsymbol{y}|} d\omega d\sigma(\boldsymbol{y}), \quad \boldsymbol{x} \in \Omega,$$

and $\mathcal{B}$ is a filter defined by

$$\mathcal{B}[g](\boldsymbol{y}, t) = \int_0^2 \frac{d^2 g}{dr^2}(\boldsymbol{y}, r) \ln(|r^2 - t^2|)\, dr, \quad \boldsymbol{y} \in \partial\Omega.$$

Note that (3.2) holds only in two dimensions. Moreover, in the Fourier domain, it reads

$$p_0(\boldsymbol{x}) = \frac{1}{(2\pi)^3}\int_{\partial\Omega}\int_{\mathbb{R}} \widehat{\mathcal{B}\mathcal{W}[p]}(\boldsymbol{y}, \omega) e^{-i\omega|\boldsymbol{x}-\boldsymbol{y}|} d\omega d\sigma(\boldsymbol{y}), \quad \boldsymbol{x} \in \Omega.$$

Hence, we introduce the Kirchhoff-Radon migration imaging functional:

$$\mathcal{I}_{\mathrm{KRM}}(\boldsymbol{x}) = \frac{1}{4\pi^2}\mathcal{R}^{\star}_{\Omega}\mathcal{B}\mathcal{W}[p](\boldsymbol{x}) = \frac{1}{2\pi}\int_{\partial\Omega}\int_{\mathbb{R}}\hat{q}(\boldsymbol{x},\omega)e^{-i\omega|\boldsymbol{x}-\boldsymbol{y}|}d\omega d\sigma(\boldsymbol{y}), \tag{3.3}$$

where

$$q = \frac{1}{4\pi^2}\mathcal{B}\mathcal{W}[p] \tag{3.4}$$

is the pre-processed data.

A second imaging functional is to simply back-project the raw data [4]:

$$\mathcal{I}_{\mathrm{KM}}(\boldsymbol{x}) = \mathcal{R}^{\star}_{\Omega}[p](\boldsymbol{x}) = \frac{1}{2\pi}\int_{\partial\Omega}\int_{\mathbb{R}}\hat{p}(\boldsymbol{y},\omega)e^{-i\omega|\boldsymbol{x}-\boldsymbol{y}|}d\omega d\sigma(\boldsymbol{y}), \quad \boldsymbol{x}\in\Omega. \tag{3.5}$$

As will be seen later, this simplified functional is sufficient for localizing point sources in homogeneous media, but may fail for imaging extended targets and/or in the presence of clutter noise.

When the sound speed varies, the phases of the measured waves are shifted according to the unknown clutter. To correct this effect, the idea of the original CINT algorithm is to back-project the space and frequency correlations between the data [6]:

$$\begin{aligned}\mathcal{I}_{\mathrm{CI}}(\boldsymbol{x}) = \; & \frac{1}{(2\pi)^2}\int_{\partial\Omega}\int_{|\boldsymbol{y}_2-\boldsymbol{y}_1|\le X_d}\int_{\mathbb{R}}\int_{|\omega_2-\omega_1|\le\Omega_d}\hat{p}(\boldsymbol{y}_1,\omega_1)e^{-i\omega_1|\boldsymbol{x}-\boldsymbol{y}_1|} \\ & \times\overline{\hat{p}}(\boldsymbol{y}_2,\omega_2)e^{i\omega_2|\boldsymbol{x}-\boldsymbol{y}_2|}d\omega_1 d\omega_2 d\sigma(\boldsymbol{y}_1)d\sigma(\boldsymbol{y}_2).\end{aligned} \tag{3.6}$$

Note that, when $\Omega_d\to\infty$ and $X_d\to\infty$, then $\mathcal{I}_{\mathrm{CI}}$ is the square of the Kirchhoff migration functional:

$$\mathcal{I}_{\mathrm{CI}}(\boldsymbol{x}) = |\mathcal{I}_{\mathrm{KM}}(\boldsymbol{x})|^2.$$

The purpose of the CINT imaging functional is to keep in (3.6) the pairs $(\boldsymbol{y}_1,\omega_1)$ and $(\boldsymbol{y}_2,\omega_2)$ for which the data $\hat{p}(\boldsymbol{y}_1,\omega_1)$ and $\hat{p}(\boldsymbol{y}_2,\omega_2)$ are coherent and to remove the pairs that do not bring information. As will be shown later, $\mathcal{I}_{\mathrm{CI}}$ is quite efficient in localizing point sources in cluttered media but not in finding the true value of p_0. Moreover, when the support of the initial pressure p_0 is extended, $\mathcal{I}_{\mathrm{CI}}$ may fail in recovering a good photoacoustic image. We propose two things. First, in order to avoid numerical oscillatory effects, we replace the sharp cut-offs in the integral by Gaussian convolutions. Then instead of taking the correlations between the back-projected raw data, we pre-process them like we do for the Radon inversion. We thus get the following CINT-Radon imaging functional:

$$\begin{aligned}\mathcal{I}_{\mathrm{CIR}}(\boldsymbol{x}) = \; & \frac{1}{(2\pi)^2}\int_{\partial\Omega}\int_{\partial\Omega}\int_{\mathbb{R}}\int_{\mathbb{R}}e^{-\frac{(\omega_2-\omega_1)^2}{2\Omega_d^2}}e^{-\frac{|\boldsymbol{y}_1-\boldsymbol{y}_2|^2}{2X_d^2}} \\ & \times\widehat{q}(\boldsymbol{y}_1,\omega_1)e^{-i\omega_1|\boldsymbol{x}-\boldsymbol{y}_1|}\overline{\widehat{q}}(\boldsymbol{y}_2,\omega_2)e^{i\omega_2|\boldsymbol{x}-\boldsymbol{y}_2|}d\omega_1 d\omega_2 d\sigma(\boldsymbol{y}_1)d\sigma(\boldsymbol{y}_2),\end{aligned} \tag{3.7}$$

where q is given by (3.4). Note again that, when $\Omega_d\to\infty$ and $X_d\to\infty$, then $\mathcal{I}_{\mathrm{CIR}}$ is the square of the Kirchhoff-Radon migration functional:

$$\mathcal{I}_{\mathrm{CIR}}(\boldsymbol{x}) = |\mathcal{I}_{\mathrm{KRM}}(\boldsymbol{x})|^2.$$

The purpose of the CINT-Radon imaging functional is to keep in (3.7) the pairs $(\boldsymbol{y}_1,\omega_1)$ and $(\boldsymbol{y}_2,\omega_2)$ for which the pre-processed data $\hat{q}(\boldsymbol{y}_1,\omega_1)$ and $\hat{q}(\boldsymbol{y}_2,\omega_2)$ are coherent and to remove the pairs that do not bring information.

4 Stability and Resolution Analysis

4.1 Noise Model

We assume that the operating bandwidth of the sensors is of the form $[\omega_0 - B/2, \omega_0 + B/2]$ with $B \ll \omega_0$ and consider the following noise model. We assume that there is an error $\nu(\boldsymbol{x}, \boldsymbol{y})$ between the theoretical travel time $\tau_0(\boldsymbol{x}, \boldsymbol{y})$ with the background velocity c_0 and the real travel time $\tau(\boldsymbol{x}, \boldsymbol{y})$ where $\boldsymbol{y}$ is a point of the surface of the observation disk $\partial\Omega$ and $\boldsymbol{x}$ is a point of the search domain. Therefore, we have

$$\tau(\boldsymbol{x}, \boldsymbol{y}) = \tau_0(\boldsymbol{x}, \boldsymbol{y}) + \nu(\boldsymbol{x}, \boldsymbol{y}),$$

where $\nu(\boldsymbol{x}, \boldsymbol{y})$ is a random process. This model can be used in the presence of low-frequency (*i.e.*, $x_c \gg 2\pi c_0/\omega_0$) cluttered noise $\mu(\boldsymbol{x})$ in (2.1) which induces perturbations to travel times up to leading order:

$$\nu(\boldsymbol{x}, \boldsymbol{y}) = -\frac{\sigma_c |\boldsymbol{y} - \boldsymbol{x}|}{2c_0} \int_0^1 \mu\Big(\frac{\boldsymbol{x} + (\boldsymbol{y} - \boldsymbol{x})s}{x_c}\Big) ds. \tag{4.1}$$

This is the so-called geometrical optics perturbations method [18, Chapter 1] that allows us to analyze the effect of random fluctuations of the sound speed on the resolution and statistical stability of the imaging functionals. This method was developed in [18, Chapter 1] to compute statistics of the travel times and other quantities that characterize wave propagation in random media.

Assuming that the search window is relatively small we can assume that ν depends only on the sensor position $\boldsymbol{y}$ and we can neglect the variations of ν with respect to $\boldsymbol{x}$. This is perfectly correct if we analyze the expectations and the variances of the imaging functionals for a fixed test point $\boldsymbol{x}$ (then the search region is just one point). This is still correct if we analyze the covariance of the imaging functional for a pair of test points $\boldsymbol{x}$ and $\boldsymbol{x}'$ that are close to each other (closer than the correlation radius x_c of the clutter noise). This model can also be used when the positions of the sensors are poorly characterized.

We assume that the random process μ is a random process with Gaussian statistics, mean zero, and covariance function:

$$\mathbb{E}\big[\sigma_c \mu\big(\frac{\boldsymbol{x}}{x_c}\big) \sigma_c \mu\big(\frac{\boldsymbol{x}'}{x_c}\big)\big] = \sigma_c^2 \exp\Big(-\frac{|\boldsymbol{x} - \boldsymbol{x}'|^2}{2x_c^2}\Big).$$

Using (4.1) and $x_c \ll X_0$ we find that ν is a random process with Gaussian statistics, mean zero, and covariance function:

$$\mathbb{E}[\nu(\boldsymbol{y})\nu(\boldsymbol{y}')] = \tau_c^2 \psi\big(\frac{|\boldsymbol{y} - \boldsymbol{y}'|}{x_c}\big), \qquad \psi(r) = \frac{1}{r}\int_0^r \exp\big(-\frac{s^2}{2}\big) ds, \tag{4.2}$$

where $\tau_c^2 = \sqrt{2\pi}\sigma_c^2 l X_0/(4c_0^2)$ is the variance of the fluctuations of the travel times. Here $\mathbb{E}$ stands for the expectation (mean value).

Using the Gaussian statistics it is straightforward to compute the moments

$$\begin{aligned}
\mathbb{E}[e^{i\omega\nu(\boldsymbol{y})}] &= \exp\Big(-\frac{\omega^2\tau_c^2}{2}\Big), \\
\mathbb{E}[e^{i\omega\nu(\boldsymbol{y}) - i\omega'\nu(\boldsymbol{y}')}] &= \exp\Big(-\frac{(\omega - \omega')^2\tau_c^2}{2} - \omega\omega'\tau_c^2\big(1 - \psi\big(\frac{|\boldsymbol{y} - \boldsymbol{y}'|}{x_c}\big)\big)\Big).
\end{aligned}$$

If we assume that $\omega_0\tau_c \gg 1$, then for $\omega, \omega' \in [\omega_0 - B/2, \omega_0 + B/2]$, we have

$$\mathbb{E}[e^{i\omega\nu(\boldsymbol{y})}] \simeq \exp\Big(-\frac{\omega_0^2\tau_c^2}{2}\Big), \tag{4.3}$$

$$\mathbb{E}[e^{i\omega\nu(\boldsymbol{y})-i\omega'\nu(\boldsymbol{y}')}] \simeq \exp\Big(-\frac{(\omega-\omega')^2\tau_c^2}{2} - \frac{|\boldsymbol{y}-\boldsymbol{y}'|^2}{2X_c^2}\Big), \tag{4.4}$$

with $X_c^2 = 3x_c^2/(2\omega_0^2\tau_c^2)$.

4.2 Kirchhoff-Radon Migration

Recall that the Kirchhoff-Radon migration functional is

$$\mathcal{I}_{\rm KRM}(\boldsymbol{x}) = \frac{1}{2\pi}\int_{\partial\Omega}\int_{\mathbb{R}} \hat{q}(\boldsymbol{y},\omega)e^{-i\omega|\boldsymbol{y}-\boldsymbol{x}|}d\omega d\sigma(\boldsymbol{y}) = \int_{\partial\Omega} q(\boldsymbol{y},|\boldsymbol{y}-\boldsymbol{x}|)d\sigma(\boldsymbol{y}), \tag{4.5}$$

where $q = \mathcal{B}\mathcal{W}[p]/(4\pi^2)$. The functional applied to the perfect pre-processed data

$$q^{(0)} = \frac{1}{4\pi^2}\mathcal{B}\mathcal{W}[p^{(0)}] \tag{4.6}$$

is

$$\mathcal{I}^{(0)}_{\rm KRM}(\boldsymbol{x}) = \frac{1}{2\pi}\int_{\partial\Omega}\int_{\mathbb{R}} \hat{q}^{(0)}(\boldsymbol{y},\omega)e^{-i\omega|\boldsymbol{y}-\boldsymbol{x}|}d\omega d\sigma(\boldsymbol{y}) = \int_{\partial\Omega} q^{(0)}(\boldsymbol{y},|\boldsymbol{y}-\boldsymbol{x}|)d\sigma(\boldsymbol{y}), \tag{4.7}$$

and it is equal to the initial condition $p_0(\boldsymbol{x})$.

We consider the random travel time model to describe the recorded data set:

$$q(\boldsymbol{y},t) = q^{(0)}(\boldsymbol{y},t-\nu(\boldsymbol{y})). \tag{4.8}$$

We first consider the expectation of the functional. Using (4.3) we find that

$$\mathbb{E}[\mathcal{I}_{\rm KRM}(\boldsymbol{x})] = \exp\Big(-\frac{\omega_0^2\tau_c^2}{2}\Big)\mathcal{I}^{(0)}_{\rm KRM}(\boldsymbol{x}),$$

which shows that the mean functional undergoes a strong damping compared to the unperturbed functional $\mathcal{I}^{(0)}_{\rm KRM}(\boldsymbol{x})$. This phenomenon is standard when studying wave propagation in random media and is sometimes called extinction [18].

The statistics of the fluctuations can be characterized by the covariance

$$\begin{aligned}\mathbb{E}\big[\mathcal{I}_{\rm KRM}(\boldsymbol{x})\overline{\mathcal{I}_{\rm KRM}(\boldsymbol{x}')}\big] = {}& \frac{1}{(2\pi)^2}\iint_{\partial\Omega\times\partial\Omega} \hat{q}^{(0)}(\boldsymbol{y}_1,\omega_1)\overline{\hat{q}^{(0)}(\boldsymbol{y}_2,\omega_2)}e^{-i\omega_1|\boldsymbol{y}_1-\boldsymbol{x}|}e^{i\omega_2|\boldsymbol{y}_2-\boldsymbol{x}'|}\\ &\times\exp\Big(-\frac{(\omega_1-\omega_2)^2\tau_c^2}{2} - \frac{|\boldsymbol{y}_1-\boldsymbol{y}_2|^2}{2X_c^2}\Big)d\omega_1 d\sigma(\boldsymbol{y}_1)d\omega_2 d\sigma(\boldsymbol{y}_2).\end{aligned}$$

In the regime in which $\tau_c^{-1} > B$ and $X_c > X_0$ we find that the amplitude of the fluctuations is of the order of

$$\mathrm{Var}\big(\mathcal{I}_{\rm KRM}(\boldsymbol{x})\big) \sim (\mathcal{I}^{(0)}_{\rm KRM}(\boldsymbol{x}))^2.$$

Here, Var stands for the variance. In the regime in which $\tau_c^{-1} < B$ and $X_c < X_0$ we find that

$$\mathrm{Var}\big(\mathcal{I}_{\rm KRM}(\boldsymbol{x})\big) \sim (\mathcal{I}^{(0)}_{\rm KRM}(\boldsymbol{x}))^2\Big(\frac{1}{B\tau_c}\Big)\Big(\frac{X_c}{X_0}\Big).$$

Define the signal-to-noise ratio (SNR) by

$$\mathrm{SNR}_{\mathrm{KRM}} = \frac{|\mathbb{E}[\mathcal{I}_{\mathrm{KRM}}(\boldsymbol{x})]|}{\mathrm{Var}(\mathcal{I}_{\mathrm{KRM}}(\boldsymbol{x}))^{1/2}}. \tag{4.9}$$

The following holds.

Proposition 4.1 *We have*

$$\mathrm{SNR}_{\mathrm{KRM}} \sim \exp\Big(-\frac{\omega_0^2\tau_c^2}{2}\Big)\Big(1+B\tau_c\Big)^{\frac{1}{2}}\Big(1+\frac{X_0}{X_c}\Big)^{\frac{1}{2}}.$$

Note that $\mathrm{SNR}_{\mathrm{KRM}}$ is very small in this regime ($\omega_0\tau_c \gg 1$).

4.3 CINT-Radon

We consider the random travel time model (4.8). We first note that coherence in (3.7) is maintained as long as $\exp(i\omega_2\nu(\boldsymbol{y}_2) - i\omega_1\nu(\boldsymbol{y}_1))$ is close to one. From (4.4) this requires that $|\omega_1-\omega_2| < \tau_c^{-1}$ and $|\boldsymbol{y}_1-\boldsymbol{y}_2| < X_c$. We can therefore anticipate that the cut-off parameters X_d and Ω_d should be related to the coherence parameters X_c and τ_c^{-1}. In the following we study the role of the cut-off parameters X_d and Ω_d for resolution and stability. For doing so, we compute the expectation and variance of the imaging functional $\mathcal{I}_{\mathrm{CIR}}$.

We have

$$\begin{aligned}\mathbb{E}[\mathcal{I}_{\mathrm{CIR}}(\boldsymbol{x})] = \frac{1}{(2\pi)^2}\iint d\omega_1 d\omega_2 \iint_{\partial\Omega\times\partial\Omega} d\sigma(\boldsymbol{y}_1)d\sigma(\boldsymbol{y}_2)\hat{q}^{(0)}(\boldsymbol{y}_1,\omega_1)\overline{\hat{q}^{(0)}(\boldsymbol{y}_2,\omega_2)}\\ \times e^{-i\omega_1|\boldsymbol{y}_1-\boldsymbol{x}|}e^{i\omega_2|\boldsymbol{y}_2-\boldsymbol{x}|}\exp\Big(-\frac{(\omega_1-\omega_2)^2}{2}(\tau_c^2+\frac{1}{\Omega_d^2}) - \frac{|\boldsymbol{y}_1-\boldsymbol{y}_2|^2}{2}(\frac{1}{X_d^2}+\frac{1}{X_c^2})\Big),\end{aligned}$$

where $q^{(0)}$ is the perfect pre-processed data defined by (4.6). Using the change of variables

$$\omega_1 = \omega_a + \frac{h_a}{2}, \quad \omega_2 = \omega_a - \frac{h_a}{2}, \qquad \boldsymbol{y}_1 = \boldsymbol{Y}_a + \frac{\boldsymbol{y}_a}{2}, \quad \boldsymbol{y}_2 = \boldsymbol{Y}_a - \frac{\boldsymbol{y}_a}{2},$$

the expectation of the CINT-Radon functional can be written as

$$\begin{aligned}\mathbb{E}[\mathcal{I}_{\mathrm{CIR}}(\boldsymbol{x})] &= \frac{1}{(2\pi)^2}\int_{\partial\Omega} d\sigma(\boldsymbol{Y}_a)\int dh_a \int_{\boldsymbol{Y}_a^\perp} d\sigma(\boldsymbol{y}_a)\hat{Q}(\boldsymbol{Y}_a,h_a,\boldsymbol{y}_a;\boldsymbol{x})\\ &\quad\times\exp\Big(-\frac{h_a^2}{2}(\tau_c^2+\frac{1}{\Omega_d^2}) - \frac{|\boldsymbol{y}_a|^2}{2}(\frac{1}{X_d^2}+\frac{1}{X_c^2})\Big),\end{aligned} \tag{4.10}$$

where

$$\boldsymbol{Y}_a^\perp = \Big\{\boldsymbol{y}_a \in \mathbb{R}^2\,,\, \boldsymbol{Y}_a - \frac{\boldsymbol{y}_a}{2} \in \partial\Omega \text{ and } \boldsymbol{Y}_a + \frac{\boldsymbol{y}_a}{2} \in \partial\Omega\Big\}$$

and

$$\begin{aligned}\hat{Q}(\boldsymbol{Y}_a,h_a,\boldsymbol{y}_a;\boldsymbol{x}) &= \int d\omega_a \hat{q}^{(0)}(\boldsymbol{Y}_a+\frac{\boldsymbol{y}_a}{2},\omega_a+\frac{h_a}{2})\overline{\hat{q}^{(0)}(\boldsymbol{Y}_a-\frac{\boldsymbol{y}_a}{2},\omega_a-\frac{h_a}{2})}\\ &\quad\times e^{-i(\omega_a+\frac{h_a}{2})|\boldsymbol{Y}_a+\frac{\boldsymbol{y}_a}{2}-\boldsymbol{x}|}e^{i(\omega_a-\frac{h_a}{2})|\boldsymbol{Y}_a-\frac{\boldsymbol{y}_a}{2}-\boldsymbol{x}|}.\end{aligned}$$

We assume that X_d is much smaller than X_0, so that $\boldsymbol{y}_1 - \boldsymbol{y}_2$ is approximately orthogonal to $(\boldsymbol{y}_1 + \boldsymbol{y}_2)/2$ when $\boldsymbol{y}_1, \boldsymbol{y}_2 \in \partial\Omega$ and $|\boldsymbol{y}_1 - \boldsymbol{y}_2| \leq X_d$. Then

$$\boldsymbol{Y}_a^{\perp} = \{\boldsymbol{y}_a \in \mathbb{R}^2\,,\, \boldsymbol{Y}_a \cdot \boldsymbol{y}_a = 0\},$$

and

$$\begin{aligned}
\hat{Q}(\boldsymbol{Y}_a, h_a, \boldsymbol{y}_a; \boldsymbol{x}) &\simeq \int d\omega_a \hat{q}^{(0)}(\boldsymbol{Y}_a + \frac{\boldsymbol{y}_a}{2}, \omega_a + \frac{h_a}{2}) \overline{\hat{q}^{(0)}(\boldsymbol{Y}_a - \frac{\boldsymbol{y}_a}{2}, \omega_a - \frac{h_a}{2})} \\
&\quad \times e^{i\omega_a \frac{\boldsymbol{x}-\boldsymbol{Y}_a}{|\boldsymbol{x}-\boldsymbol{Y}_a|}\cdot \boldsymbol{y}_a - i h_a |\boldsymbol{x}-\boldsymbol{Y}_a|} \\
&\simeq \frac{1}{(2\pi)^2} \int d\omega_a \int d\tau_a \int_{\boldsymbol{Y}_a^{\perp}} d\sigma(\boldsymbol{\kappa}_a) \mathcal{W}_q(\boldsymbol{Y}_a, \omega_a; \boldsymbol{\kappa}_a, \tau_a) \\
&\quad \times e^{i(\omega_a \frac{\boldsymbol{x}-\boldsymbol{Y}_a}{|\boldsymbol{x}-\boldsymbol{Y}_a|} - \boldsymbol{\kappa}_a)\cdot \boldsymbol{y}_a + (\tau_a - |\boldsymbol{x}-\boldsymbol{Y}_a|) h_a},
\end{aligned}$$

where $\mathcal{W}_q$ is the Wigner transform of $q^{(0)}$:

$$\begin{aligned}
\mathcal{W}_q(\boldsymbol{Y}_a, \omega_a; \boldsymbol{\kappa}_a, \tau_a) &= \int dh_a \int_{\boldsymbol{Y}_a^{\perp}} d\sigma(\boldsymbol{y}_a) \hat{q}^{(0)}(\boldsymbol{Y}_a + \frac{\boldsymbol{y}_a}{2}, \omega_a + \frac{h_a}{2}) \overline{\hat{q}^{(0)}(\boldsymbol{Y}_a - \frac{\boldsymbol{y}_a}{2}, \omega_a - \frac{h_a}{2})} \\
&\quad \times e^{i\boldsymbol{\kappa}_a \cdot \boldsymbol{y}_a - i h_a \tau_a}. \qquad (4.11)
\end{aligned}$$

Therefore, we get

$$\begin{aligned}
\mathbb{E}[\mathcal{I}_{\mathrm{CIR}}(\boldsymbol{x})] &= \frac{1}{(2\pi)^3 (\frac{1}{X_d^2} + \frac{1}{X_c^2})^{\frac{1}{2}} (\tau_c^2 + \frac{1}{\Omega_d^2})^{\frac{1}{2}}} \int_{\partial\Omega} d\sigma(\boldsymbol{Y}_a) \int d\omega_a \int_{\boldsymbol{Y}_a^{\perp}} d\sigma(\boldsymbol{\kappa}_a) \int d\tau_a \\
&\quad \times \mathcal{W}_q(\boldsymbol{Y}_a, \omega_a; \boldsymbol{\kappa}_a, \tau_a) \\
&\quad \times \exp\Big(- \frac{\big|\boldsymbol{\kappa}_a - \omega_a\big(\frac{\boldsymbol{x}-\boldsymbol{Y}_a}{|\boldsymbol{x}-\boldsymbol{Y}_a|} - (\frac{\boldsymbol{Y}_a}{|\boldsymbol{Y}_a|} \cdot \frac{\boldsymbol{x}-\boldsymbol{Y}_a}{|\boldsymbol{x}-\boldsymbol{Y}_a|}) \frac{\boldsymbol{Y}_a}{|\boldsymbol{Y}_a|}\big)\big|^2}{2(\frac{1}{X_d^2} + \frac{1}{X_c^2})} - \frac{(\tau_a - |\boldsymbol{Y}_a - \boldsymbol{x}|)^2}{2(\tau_c^2 + \frac{1}{\Omega_d^2})} \Big).
\end{aligned}$$

Since, for any s,

$$\mathcal{W}_q(\boldsymbol{Y}_a, \omega_a; \boldsymbol{\kappa}_a + s\boldsymbol{Y}_a, \tau_a) = \mathcal{W}_q(\boldsymbol{Y}_a, \omega_a; \boldsymbol{\kappa}_a, \tau_a),$$

we obtain the following result.

Proposition 4.2 *We have*

$$\begin{aligned}
\mathbb{E}[\mathcal{I}_{\mathrm{CIR}}(\boldsymbol{x})] &= \frac{1}{(2\pi)^3 (\frac{1}{X_d^2} + \frac{1}{X_c^2})^{\frac{1}{2}} (\tau_c^2 + \frac{1}{\Omega_d^2})^{\frac{1}{2}}} \int_{\partial\Omega} d\sigma(\boldsymbol{Y}_a) \int d\omega_a \int_{\boldsymbol{Y}_a^{\perp}} d\sigma(\boldsymbol{\kappa}_a) \int d\tau_a \\
&\quad \times \mathcal{W}_q(\boldsymbol{Y}_a, \omega_a; \boldsymbol{\kappa}_a, \tau_a) \exp\Big(- \frac{\big|\boldsymbol{\kappa}_a - \omega_a \frac{\boldsymbol{x}-\boldsymbol{Y}_a}{|\boldsymbol{x}-\boldsymbol{Y}_a|}\big|^2}{2(\frac{1}{X_d^2} + \frac{1}{X_c^2})} - \frac{(\tau_a - |\boldsymbol{Y}_a - \boldsymbol{x}|)^2}{2(\tau_c^2 + \frac{1}{\Omega_d^2})} \Big). \qquad (4.12)
\end{aligned}$$

Formula (4.12) shows that the coherent part (*i.e.*, the expectation) of the CINT-Radon functional is a smoothed version of the Wigner transform of the pre-processed data. It selects a band of directions and time delays that are centered around the direction and the time delay between the search point $\boldsymbol{x}$ and the point $\boldsymbol{Y}_a$ of the sensor array.

We observe that:

- if $\Omega_d > \tau_c^{-1}$ and $X_d > X_c$ then the cut-off parameters Ω_d and X_d have no influence on the coherent part of the functional which does not depend on (Ω_d, X_d).
- if $\Omega_d < \tau_c^{-1}$ and $X_d < X_c$ then CINT has an influence and reduces the resolution of the coherent part of the functional (it enhances the smoothing of the Wigner transform).

We next compute the covariance of the CINT-Radon functional. If

$$\omega_1 = \omega_a + \frac{h_a}{2}, \quad \omega_2 = \omega_a - \frac{h_a}{2}, \qquad \omega_3 = \omega_b + \frac{h_b}{2}, \quad \omega_4 = \omega_b - \frac{h_b}{2},$$
$$\boldsymbol{y}_1 = \boldsymbol{Y}_a + \frac{\boldsymbol{y}_a}{2}, \quad \boldsymbol{y}_2 = \boldsymbol{Y}_a - \frac{\boldsymbol{y}_a}{2}, \qquad \boldsymbol{y}_3 = \boldsymbol{Y}_b + \frac{\boldsymbol{y}_b}{2}, \quad \boldsymbol{y}_4 = \boldsymbol{Y}_b - \frac{\boldsymbol{y}_b}{2},$$

then

$$\mathbb{E}\big[e^{i\omega_1\nu(\boldsymbol{y}_1)-i\omega_2\nu(\boldsymbol{y}_2)}\overline{e^{i\omega_3\nu(\boldsymbol{y}_3)-i\omega_4\nu(\boldsymbol{y}_4)}}\big] \simeq \exp\Big(-\frac{(h_a-h_b)^2\tau_c^2}{2} - \frac{|\boldsymbol{y}_a-\boldsymbol{y}_b|^2}{2X_c^2}\Big),$$

and therefore,

$$\begin{aligned}\mathbb{E}\big[\mathcal{I}_{\rm CIR}(\boldsymbol{x})\overline{\mathcal{I}_{\rm CIR}(\boldsymbol{x}')}\big] &= \frac{1}{(2\pi)^4}\iiint d\sigma(\boldsymbol{Y}_a)dh_a d\sigma(\boldsymbol{y}_a)d\sigma(\boldsymbol{Y}_b)dh_b d\sigma(\boldsymbol{y}_b)\\ &\quad\times\hat{Q}(\boldsymbol{Y}_a,h_a,\boldsymbol{y}_a;\boldsymbol{x})\overline{\hat{Q}(\boldsymbol{Y}_b,h_b,\boldsymbol{y}_b;\boldsymbol{x}')}\\ &\quad\times\exp\Big(-\frac{(h_a^2+h_b^2)}{2\Omega_d^2} - \frac{(|\boldsymbol{y}_a|^2+|\boldsymbol{y}_b|^2)}{2X_d^2}\Big)\\ &\quad\times\exp\Big(-\frac{(h_a-h_b)^2\tau_c^2}{2} - \frac{|\boldsymbol{y}_a-\boldsymbol{y}_b|^2}{2X_c^2}\Big).\end{aligned}$$

Using (4.10) we can see that, if $\Omega_d < \tau_c^{-1}$ and $X_d < X_c$, then we have

$$\mathbb{E}[\mathcal{I}_{\rm CIR}(\boldsymbol{x})] = \frac{1}{(2\pi)^2}\iiint d\sigma(\boldsymbol{Y}_a)dh_a d\sigma(\boldsymbol{y}_a)\hat{Q}(\boldsymbol{Y}_a,h_a,\boldsymbol{y}_a;\boldsymbol{x})\exp\Big(-\frac{h_a^2}{2\Omega_d^2} - \frac{|\boldsymbol{y}_a|^2}{2X_d^2}\Big).$$

Using

$$1-\exp\Big(-\frac{(h_a-h_b)^2\tau_c^2}{2} - \frac{|\boldsymbol{y}_a-\boldsymbol{y}_b|^2}{2X_c^2}\Big) \simeq \frac{(h_a-h_b)^2\tau_c^2}{2} + \frac{|\boldsymbol{y}_a-\boldsymbol{y}_b|^2}{2X_c^2},$$

it follows that

$$\mathrm{Var}\big(\mathcal{I}_{\rm CIR}(\boldsymbol{x})\big) = \mathbb{E}\big[\big|\mathcal{I}_{\rm CIR}(\boldsymbol{x})\big|^2\big] - \big|\mathbb{E}\big[\mathcal{I}_{\rm CIR}(\boldsymbol{x})\big]\big|^2 \quad\sim\quad \Big((\Omega_d\tau_c)^2 + \big(\frac{X_d}{X_c}\big)^2\Big)\big|\mathbb{E}\big[\mathcal{I}_{\rm CIR}(\boldsymbol{x})\big]\big|^2.$$

Therefore, the following proposition, where the SNR is defined analogously to (4.9), holds.

Proposition 4.3 *When $\Omega_d < \tau_c^{-1}$ and $X_d < X_c$, we have*

$$\mathrm{SNR}_{\rm CIR} \sim \frac{1}{\sqrt{(\Omega_d\tau_c)^2 + \big(\frac{X_d}{X_c}\big)^2}}. \tag{4.13}$$

Note that the SNR is greater than one when $\Omega_d < \tau_c^{-1}$ and $X_d < X_c$.

To conclude, we notice that the values of the parameters $X_d \simeq X_c$ and $\Omega_d \simeq \tau_c^{-1}$ achieve a good trade-off between resolution and stability. When taking smaller values $\Omega_d < \tau_c^{-1}$ and $X_d < X_c$ one increases the signal-to-noise ratio but one also reduces the resolution. In practice, these parameters are difficult to estimate directly from the data, so it is better to determine them adaptively, by optimizing over Ω_d and X_d the quality of the resulting image. This is exactly what is done in adaptive CINT [7].

4.4 Two Particular Cases

We now discuss the following two particular cases:

(i) If we take $X_d \to 0$ then the CINT functional has the form

$$\mathcal{I}_{\mathrm{CIR}}(\boldsymbol{x}) = \frac{1}{(2\pi)^2}\int_{\mathbb{R}}\int_{\mathbb{R}} d\omega_1 d\omega_2 \int_{\partial\Omega} d\sigma(\boldsymbol{y}) e^{-\frac{(\omega_1-\omega_2)^2}{2\Omega_d^2}} \hat{q}(\boldsymbol{y},\omega_1) e^{-i\omega_1|\boldsymbol{y}-\boldsymbol{x}|}\overline{\hat{q}(\boldsymbol{y},\omega_2)} e^{i\omega_2|\boldsymbol{y}-\boldsymbol{x}|}. \tag{4.14}$$

This case could correspond to the situation in which X_c is very small, which means that the signals recorded by different sensors are so noisy that they are independent from each other.
If $\Omega_d > B$, then (4.14) is equivalent to the incoherent matched field functional

$$\mathcal{I}_{\mathrm{CIR}}(\boldsymbol{x}) \simeq \int_{\partial\Omega} d\sigma(\boldsymbol{Y}_a)\big|q(\boldsymbol{Y}_a, |\boldsymbol{Y}_a - \boldsymbol{x}|)\big|^2.$$

If $\Omega_d \le B$ (or, more generally, for any Ω_d), then (4.14) is a smoothed (in time) version of this functional given by

$$\mathcal{I}_{\mathrm{CIR}}(\boldsymbol{x}) \;=\; \frac{\Omega_d}{\sqrt{2\pi}}\int_{\partial\Omega} d\sigma(\boldsymbol{Y}_a)\int_{\mathbb{R}} dt\big|q(\boldsymbol{Y}_a, |\boldsymbol{Y}_a-\boldsymbol{x}|+t)\big|^2 \exp\Big(-\frac{\Omega_d^2 t^2}{2}\Big).$$

(ii) If we take $X_d \to \infty$ then the CINT functional has the form

$$\begin{aligned}\mathcal{I}_{\mathrm{CIR}}(\boldsymbol{x}) \;=\; & \frac{1}{(2\pi)^2}\int_{\mathbb{R}}\int_{\mathbb{R}} d\omega_1 d\omega_2 \iint_{\partial\Omega\times\partial\Omega} d\sigma(\boldsymbol{y}_1) d\sigma(\boldsymbol{y}_2) e^{-\frac{(\omega_1-\omega_2)^2}{2\Omega_d^2}} \\ & \times \hat{q}(\boldsymbol{y}_1,\omega_1) e^{-i\omega_1|\boldsymbol{y}_1-\boldsymbol{x}|}\overline{\hat{q}(\boldsymbol{y}_2,\omega_2)} e^{i\omega_2|\boldsymbol{y}_2-\boldsymbol{x}|}. \end{aligned} \tag{4.15}$$

This case could correspond to the situation in which X_c is very large, which means that the signals recorded by different sensors are strongly correlated with one another. This is a typical weak noise case.
If $\Omega_d > B$, then (4.14) is equivalent to the coherent matched field function (or square KRM functional):

$$\mathcal{I}_{\mathrm{CIR}}(\boldsymbol{x}) \simeq \Big|\int_{\partial\Omega} d\sigma(\boldsymbol{Y}_a) q(\boldsymbol{Y}_a, |\boldsymbol{Y}_a - \boldsymbol{x}|)\Big|^2.$$

If $\Omega_d \le B$ (or, more generally, for any Ω_d), then (4.15) is a smoothed (in time) version of this functional:

$$\mathcal{I}_{\mathrm{CIR}}(\boldsymbol{x}) \;=\; \frac{\Omega_d}{\sqrt{2\pi}}\int_{\mathbb{R}} dt\Big|\int_{\partial\Omega} d\sigma(\boldsymbol{Y}_a) q(\boldsymbol{Y}_a, |\boldsymbol{Y}_a-\boldsymbol{x}|+t)\Big|^2 \exp\Big(-\frac{\Omega_d^2 t^2}{2}\Big).$$

5 CINT-Radon Algorithm in a Bounded Domain

When considering photoacoustics in a bounded domain, we developed in [3] an approach involving the line Radon transform of the initial condition. We will consider homogeneous Dirichlet conditions:

$$\begin{cases} \dfrac{\partial^2 p}{\partial t^2}(\boldsymbol{x},t) - c(\boldsymbol{x})^2 \Delta p(\boldsymbol{x},t) = 0, \quad \boldsymbol{x}\in\Omega, \\ p(\boldsymbol{x},0) = p_0(\boldsymbol{x}), \qquad \dfrac{\partial p}{\partial t}(\boldsymbol{x},0) = 0, \quad \boldsymbol{x}\in\Omega, \\ p(\boldsymbol{y},t) = 0, \quad \boldsymbol{y}\in\partial\Omega. \end{cases}$$

Here, Ω is not necessarily a disk. Let $\boldsymbol{n}$ denote the outward normal to $\partial\Omega$. When $c(\boldsymbol{x}) = c_0$, we can express the line Radon transform of the initial condition $p_0(\boldsymbol{x})$ in terms of the Neumann measurements $\partial_n p(\boldsymbol{y}, t) = \boldsymbol{n}(\boldsymbol{y}) \cdot \boldsymbol{\nabla} p(\boldsymbol{y}, t)$ on $\partial\Omega \times [0, T]$:

$$\mathcal{R}[p_0](\boldsymbol{\theta}, s) = \mathcal{W}[\partial_n p](\boldsymbol{\theta}, s),$$

where the line Radon transform is defined by

$$\mathcal{R}[p_0](\boldsymbol{\theta}, r) := \int_{\mathbb{R}} p_0(r\boldsymbol{\theta} + s\boldsymbol{\theta}^{\perp}) ds, \quad \boldsymbol{\theta} \in \mathbb{S}^1, \quad r \in \mathbb{R},$$

and

$$\mathcal{W}[g](\boldsymbol{\theta}, s) := \int_0^T \int_{\partial\Omega} g(\boldsymbol{x}, t) H\left(\frac{\boldsymbol{x} \cdot \boldsymbol{\theta}}{c_0} + t - s\right) d\sigma(\boldsymbol{x}) dt, \quad \boldsymbol{\theta} \in \mathbb{S}^1, \quad s \in \mathbb{R}.$$

Here H denotes the Heaviside function. We then invert the Radon transform using the back-projection algorithm

$$p_0 = \mathcal{R}^{\star} \mathcal{B} \mathcal{W}[\partial_n p],$$

where $\mathcal{R}^{\star}$ is the adjoint Radon transform:

$$\mathcal{R}^{\star}[f](\boldsymbol{x}) = \frac{1}{2\pi} \int_{\mathbb{S}^1} f(\boldsymbol{\theta}, \boldsymbol{x} \cdot \boldsymbol{\theta}) d\sigma(\boldsymbol{\theta}) = \frac{1}{(2\pi)^2} \int_{\mathbb{S}^1} \int_{\mathbb{R}} \hat{f}(\boldsymbol{\theta}, \omega) e^{-i\omega \boldsymbol{x} \cdot \boldsymbol{\theta}} d\omega d\sigma(\boldsymbol{\theta}), \quad \boldsymbol{x} \in \Omega,$$

and $\mathcal{B}$ is a ramp filter

$$\mathcal{B}[g](\boldsymbol{\theta}, s) = \frac{1}{4\pi} \int_{\mathbb{R}} |\omega| \hat{g}(\boldsymbol{\theta}, \omega) e^{-i\omega s} d\omega, \quad \boldsymbol{\theta} \in \mathbb{S}^1.$$

Here, the hat stands for the Fourier transform (3.1) in the second (shift) variable. In the Fourier domain, the inversion reads

$$p_0(\boldsymbol{x}) = \frac{1}{(2\pi)^2} \int_{\mathbb{S}^1} \int_{\mathbb{R}} \widehat{\mathcal{B}\mathcal{W}[\partial_n p]}(\boldsymbol{\theta}, \omega) e^{-i\omega \boldsymbol{x} \cdot \boldsymbol{\theta}} d\omega d\sigma(\boldsymbol{\theta}), \quad \boldsymbol{x} \in \Omega.$$

Therefore, a natural idea to extend the CINT imaging to bounded media is to consider the imaging functional:

$$\begin{aligned} \mathcal{I}_{\mathrm{CIR}}(\boldsymbol{x}) \quad &:= \frac{1}{(2\pi)^4} \int_{\mathbb{S}^1} \int_{\mathbb{S}^1} \int_{\mathbb{R}} \int_{\mathbb{R}} e^{-\frac{(\omega_2 - \omega_1)^2}{2\Omega_d^2}} e^{-\frac{|\boldsymbol{\theta}_2 - \boldsymbol{\theta}_1|^2}{2\Theta_d^2}} \\ &\times \widehat{\mathcal{B}\mathcal{W}[\partial_n p]}(\boldsymbol{\theta}_1, \omega_1) e^{-i\omega_1 \boldsymbol{x} \cdot \boldsymbol{\theta}_1} \overline{\widehat{\mathcal{B}\mathcal{W}[\partial_n p]}}(\boldsymbol{\theta}_2, \omega_2) e^{i\omega_2 \boldsymbol{x} \cdot \boldsymbol{\theta}_2} d\omega_1 d\omega_2 d\sigma(\boldsymbol{\theta}_1) d\sigma(\boldsymbol{\theta}_2). \end{aligned}$$

The stability and resolution analysis in Section 4 applies immediately to $\mathcal{I}_{\mathrm{CIR}}$.

6 Numerical Illustrations

In this section we present numerical experiments to illustrate the performance of the CINT-Radon algorithms and to compare them with the Kirchhoff-Radon. The wave equation (direct problem) is solved via a Lie-splitting method. It can be rewritten as a first order partial differential equation:

$$\partial_t \mathbf{P} = \mathbf{A}\mathbf{P} + \mathbf{B}\mathbf{P},$$

where

$$\mathbf{P} = \begin{pmatrix} p \\ \partial_t p \end{pmatrix}, \quad \mathbf{A} = \begin{pmatrix} 0 & 1 \\ c_0^2\Delta & 0 \end{pmatrix}, \quad \text{and} \quad \mathbf{B} = \begin{pmatrix} 0 & 0 \\ (c^2 - c_0^2)\Delta & 0 \end{pmatrix}.$$

The operator $\mathbf{A}$ is solved exactly in the Fourier space while the operator $\mathbf{B}$ is treated explicitly with a finite difference method and a PML formulation in the case of free space. The inverse circular Radon formula is discretized as in [10].

In Figure 1, we consider 6 point sources which emit pulses of the form

$$f(t) = \cos(2\pi\omega_0 t)t\delta_\omega \exp(-\pi t^2\delta_\omega^2), \quad \text{with} \quad \delta_\omega = 10, \quad \omega_0 = 3\delta_\omega.$$

We use the random velocity c_1, visualized in Figure 1. Figure 2 presents the pressure $p(\boldsymbol{y}, t)$ computed without and with noise, and the reconstruction of the source locations obtained by the Kirchhoff migration functional $\mathcal{I}_{\text{KM}}$. Figure 2 illustrates that in the presence of noise, $\mathcal{I}_{\text{KM}}$ becomes very instable and fails to really localize the targets. The images obtained by $\mathcal{I}_{\text{CI}}$ are plotted in Figure 3 and compared to those obtained by $\mathcal{I}_{\text{KM}}$. Note that $\mathcal{I}_{\text{CI}}$ presents better stability properties when X_d and Ω_d become small as predicted by the theory.

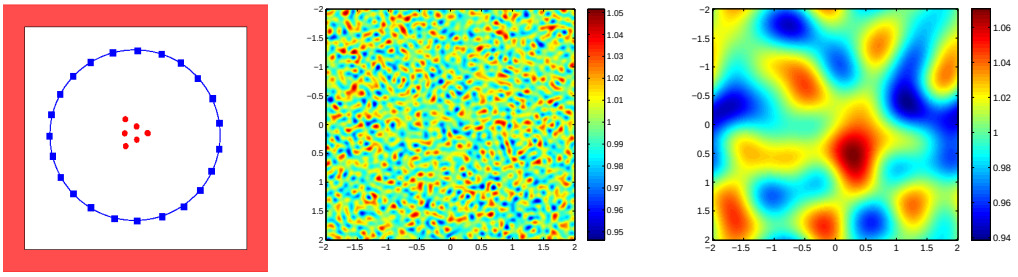

Figure 1: Left: positions of the sensors; center: random velocity c_1 with high frequencies; right: random velocity c_2 with low frequencies.

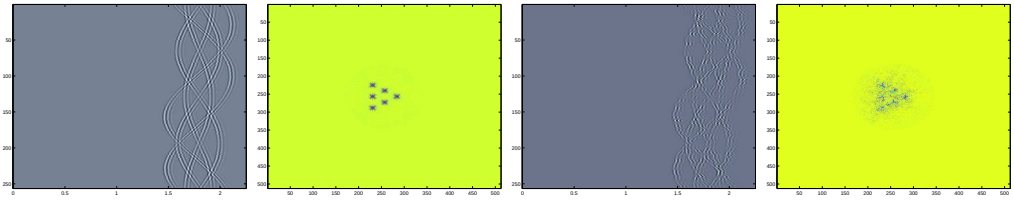

Figure 2: Test1: measured data $p(\boldsymbol{y}, t)$ and source localization using Kirchhoff migration $\mathcal{I}_{\text{KM}}$ with (right) and without (left) noise.

We now consider the case of extended targets and test the imaging functional $\mathcal{I}_{\text{CIR}}$. We use the random velocity c_2 shown in Figure 1. Reconstructions of the initial pressure obtained by $\mathcal{I}_{\text{KRM}}$ are plotted in Figures 4 and 6. Figures 4 and 6 clearly highlight the fact that the noise significantly affects the reconstruction. In fact, the whole line is not found.

On the other hand, plots of $\mathcal{I}_{\text{CIR}}$ presented in Figures 5 and 7 provide more stable reconstructions of $p_0(\boldsymbol{x})$. However, note that choosing small values of the parameters X_d and Ω_d can affect the reconstruction in the sense that $\mathcal{I}_{\text{CIR}}$ becomes very different from the

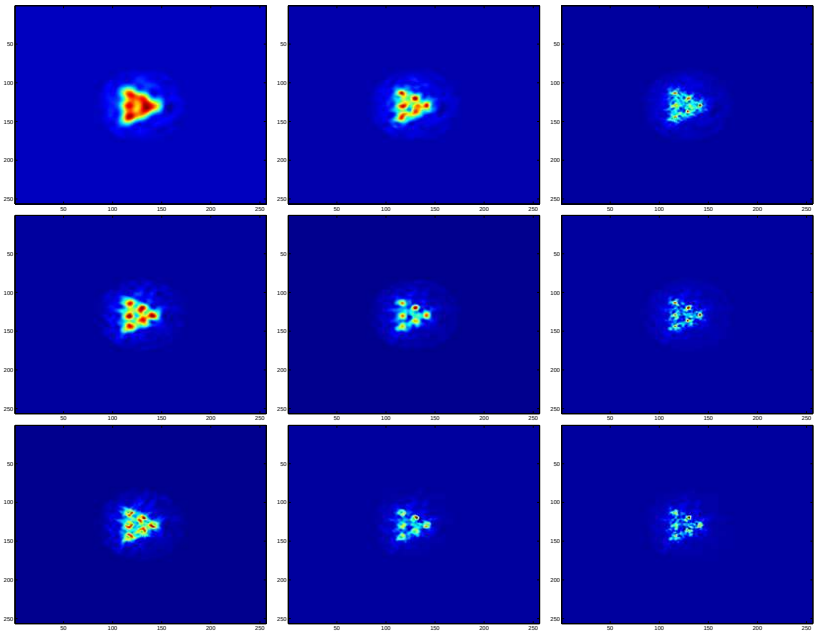

Figure 3: Test1: source localization using the standard CINT functional $\mathcal{I}_{\mathrm{CI}}$, with parameters X_d and Ω_d given by $X_d = 0.25, 0.5, 1$ (from left to right) and $\Omega_d = 25, 50, 100$ (from top to bottom).

expected value, p_0^2, when X_d and Ω_d tend to zero. This is a manifestation of the trade-off between resolution and stability discussed in Section 4.

In the case of a bounded domain, we consider the low frequency cluttered speed of Figure 1, on a square medium, with homogeneous Dirichlet conditions. We illustrate the performance of $\mathcal{I}_{\mathrm{CIR}}$ on the Shepp-Logan phantom. Figure 8 shows the reconstruction using the inverse Radon transform algorithm. We notice that the outer interface appears twice. In fact, $\mathcal{I}_{\mathrm{CIR}}$ can correct this effect. Figure 9 shows results for different values of Θ_d and Ω_d. The imaging functional $\mathcal{I}_{\mathrm{CIR}}$ can get the outer interface correctly but seems to focus too much on it. To check if $\mathcal{I}_{\mathrm{CIR}}$ reconstructs the inside of the target with the good contrast, we show in Figure 10 the same images with a colormap saturated at 80% of their maximum values.

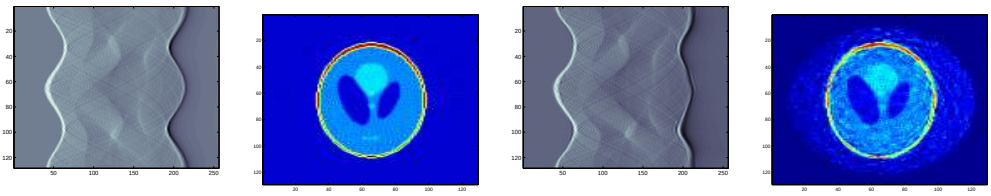

Figure 4: Test2: measured data $p(\boldsymbol{y}, t)$ and reconstruction of $p_0(\boldsymbol{x})$ using $\mathcal{I}_{\mathrm{KRM}}$ with (right) and without (left) noise.

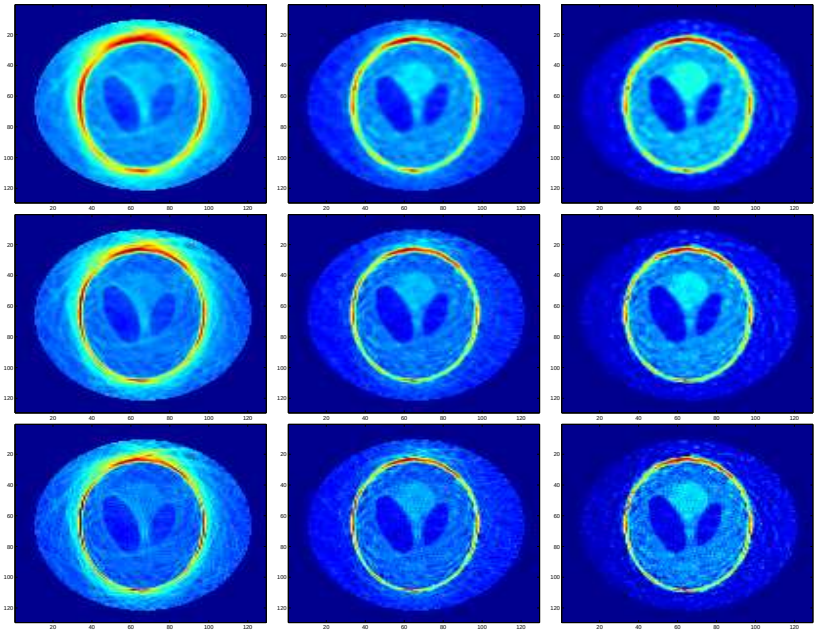

Figure 5: Test2: source localization using $\mathcal{I}_{\mathrm{CIR}}$, with X_d and Ω_d given by $X_d = 0.5, 1, 2$ (from left to right) and $\Omega_d = 50, 100, 200$ (from top to bottom).

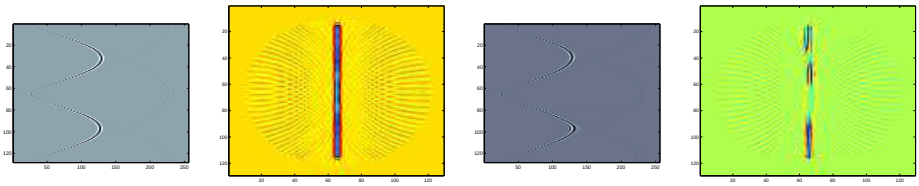

Figure 6: Test3: measured data $p(\boldsymbol{y}, t)$ and reconstruction of p_0 using $\mathcal{I}_{\mathrm{KRM}}$ with (right) and without (left) noise.

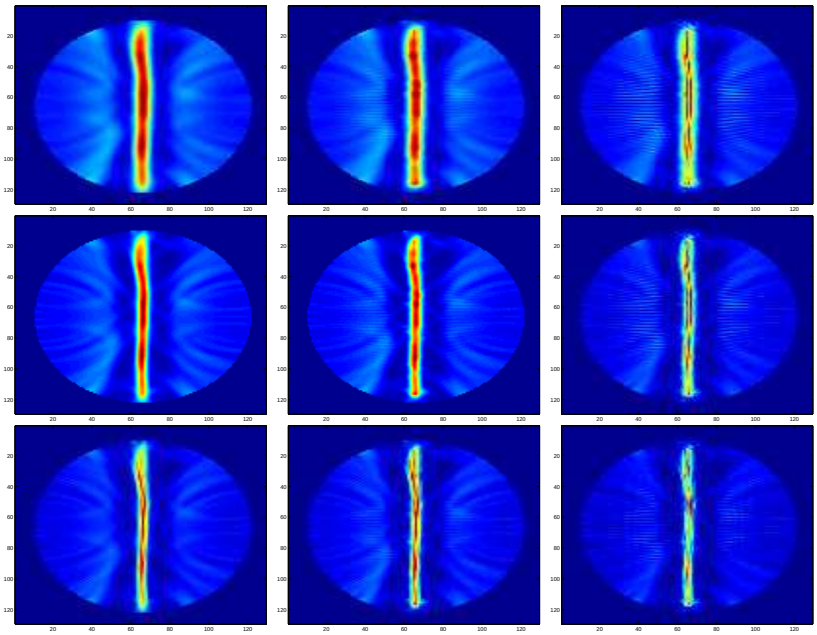

Figure 7: Test3 : source localization using $\mathcal{I}_{\mathrm{CIR}}$, with X_d and Ω_d given by $X_d = 0.5, 1, 2$ (from left to right) and $\Omega_d = 50, 100, 200$ (from top to bottom).

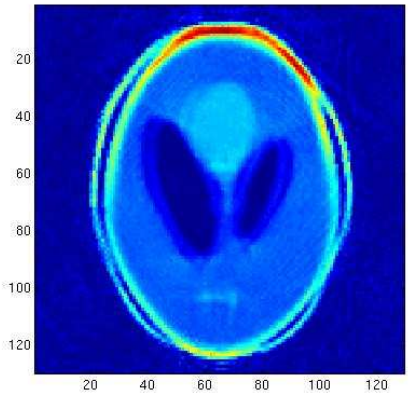

Figure 8: Reconstruction of an extended target using line Radon transform in the case of imposed boundary conditions.

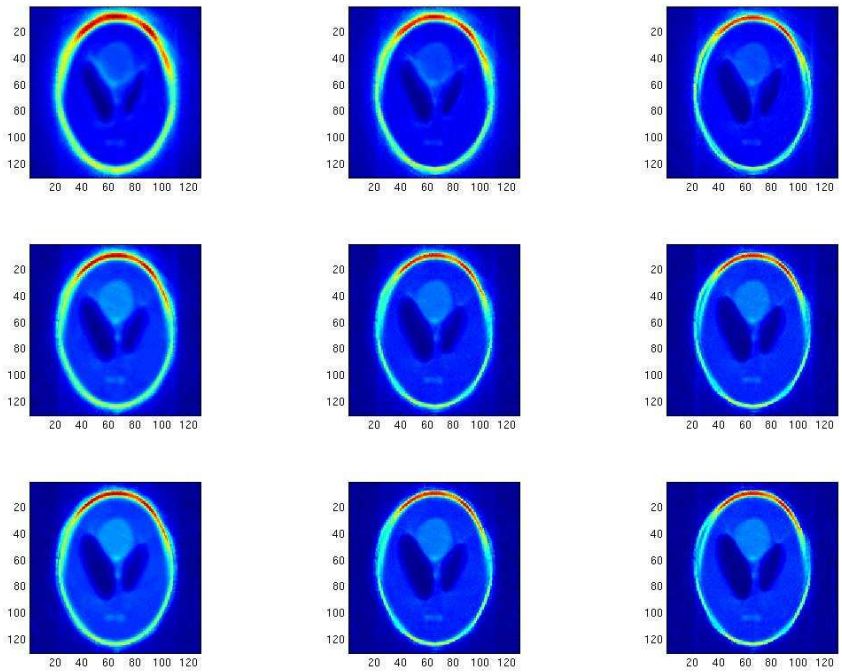

Figure 9: Extended target reconstruction with boundary conditions using $\mathcal{I}_{\mathrm{CIR}}$, with Θ_d and Ω_d given by $\Theta_d = 1, 3, 6$ (from top to bottom) and $\Omega_d = 50, 100, 200$ (from left to right).

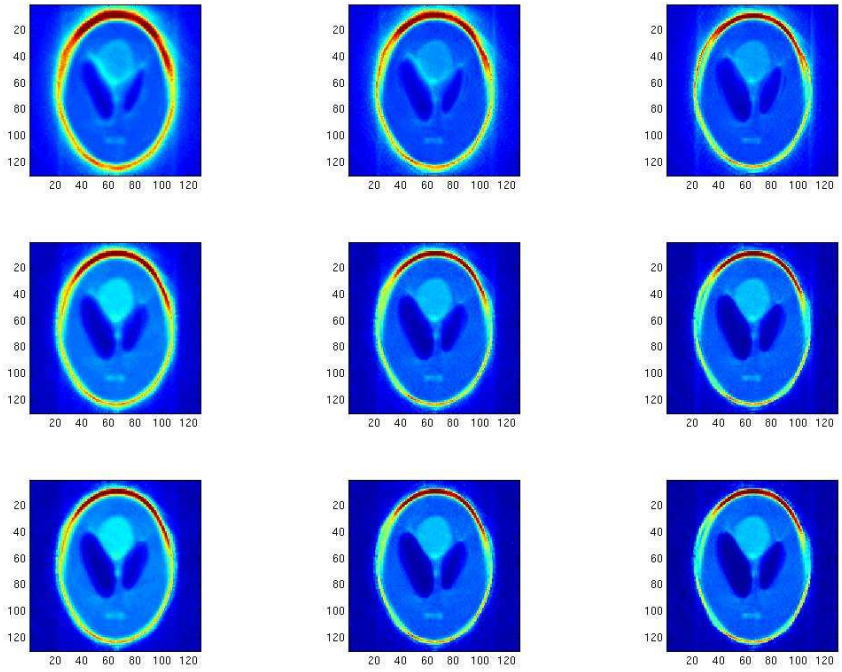

Figure 10: Extended target reconstruction with boundary conditions using $\mathcal{I}_{\mathrm{CIR}}$, with Θ_d and Ω_d given by $\Theta_d = 1, 3, 6$ (from top to bottom) and $\Omega_d = 50, 100, 200$ (from left to right). Colormaps are saturated at 80% of the maximum values of the images.

7 Conclusion

In this paper we have introduced new CINT-Radon type imaging functionals in order to correct the effect on photoacoustic images of random fluctuations of the background sound speed around a known constant value. We have provided a stability and resolution analysis of the proposed algorithms and found the values of the cut-off parameters which achieve a good trade-off between resolution and stability. We have presented numerical reconstructions of both small and extended targets and compared our algorithms with Kirchhoff-Radon migration functionals. The CINT-Radon imaging functionals give better reconstruction than Kirchhoff-Radon migration, specially for extended targets in the presence of low-frequency medium noise.

References

[1] H. Ammari, E. Bossy, V. Jugnon, and H. Kang, Mathematical modelling in photoacoustic imaging of small absorbers, SIAM Rev., to appear.

[2] H. Ammari, E. Bossy, V. Jugnon, and H. Kang, Reconstruction of the optical absorption coefficient of a small absorber from the absorbed energy density, SIAM J. Appl. Math., to appear.

[3] H. Ammari, E. Bretin, V. Jugnon, and A. Wahab, Photoacoustic imaging for attenuating acoustic media, in *Mathematical Modeling in Biomedical Imaging II*, Lecture Notes in Mathematics, Springer-Verlag, Berlin, to appear.

[4] N. Bleistein, J. K. Cohen, and J. W. Stockwell Jr., *Mathematics of Multidimensional Seismic Imaging, Migration, and Inversion*, Springer, New York, 2001.

[5] L. Borcea, G. Papanicolaou, and C. Tsogka, Theory and applications of time reversal and interferometric imaging, Inverse Problems, 19 (2003), 134–164.

[6] L. Borcea, G. Papanicolaou, and C. Tsogka, Interferometric array imaging in clutter, Inverse Problems 21 (2005), 1419–1460.

[7] L. Borcea, G. Papanicolaou, and C. Tsogka, Adaptive interferometric imaging in clutter and optimal illumination, Inverse Problems 22 (2006), 1405–1436.

[8] L. Borcea, G. Papanicolaou, and C. Tsogka, Coherent interferometric imaging in clutter, Geophysics 71 (2006), SI165–SI175.

[9] T. K. Chan, Y. Kuga, and A. Ishimaru, Experimental studies on circular sar imaging in clutter using angular correlation function technique, IEEE Trans. Geoscience and Remote Sensing, 37 (1999), 2192–2197.

[10] D. Finch, M. Haltmeier, and Rakesh, Inversion of spherical means and the wave equation in even dimensions, SIAM J. Appl. Math., 68 (2007), 392–412.

[11] D. Finch, S. Patch, and Rakesh, Determining a function from its mean-values over a family of spheres, SIAM J. Math. Anal., 35 (2004), 1213–1240.

[12] J.-P. Fouque, J. Garnier, G. Papanicolaou, and K. Sølna, *Wave Propagation and Time Reversal in Randomly Layered Media*, Springer, New York, 2007.

[13] M. Haltmeier, O. Scherzer, P. Burgholzer, R. Nuster, and G. Paltauf, Thermoacoustic tomography and the circular Radon transform: exact inversion formula, Math. Model. Meth. Appl. Sci., 17 (2007), 635–655.

[14] M. Haltmeier, T. Schuster, and O. Scherzer, Filtered backprojection for thermoacoustic computed tomography in spherical geometry, Math. Meth. Appl. Sci., 28 (2005), 1919-1937.

[15] P. Kunchment and L. Kunyansky, Mathematics of thermoacoustic tomography, Europ. J. Appl. Math., 19 (2008), 191–224.

[16] P. Kuchment and L. Kunyansky, Mathematics of photoacoustics and thermoacoustic tomography, in *Handbook of Mathematical Methods in Imaging* (ed: O. Scherzer), Springer-Verlag, New York, 2011.

[17] L. V. Nguyen, A family of inversion formulas in thermoacoustic tomography, Inverse Problems and Imaging, 3 (2009), 649–675.

[18] S. M. Rytov, Y. A. Kravtsov, and V. I. Tatarskii, *Principles of Statistical Radiophysics. 4. Wave Propagation through Random Media*, Springer-Verlag, Berlin, 1989.

[19] R. Snieder, A. Gret, H. Douma, and J. Scales, Coda wave interferometry for estimating nonlinear behavior in seismic velocity, Science, 295 (2002), 2253–2255.

[20] G. T. Schuster, J. Yu, J. Sheng, and J. Rickett, Interferometric daylight seismic imaging, Geophysics Journal International, 157 (2004), 838–852.

[21] M. Xu and L.V. Wang, Photoacoustic imaging in biomedicine, Rev. Scient. Instrum., 77 (2006), 041101.